Predictive Nanoscale Simulations for the THz Regime

Ulrik G. Vej-Hansen*
Synopsys Denmark Aps
Copenhagen, Denmark
ulrik.vej-hansen@synopsys.com

Kevin Galiano*
Northrop Grumman Corporation
Baltimore, MD, USA
kevin.galiano@ngc.com

Nelson de Almeida Braga
Synopsys, Inc
San Diego, CA, USA
nelson.braga@synopsys.com

Tony Riccobono
Synopsys, Inc
Los Angeles, CA, USA
tony.riccobono@synopsys.com

Thomas J. Knight
Northrop Grumman Corporation
Baltimore, MD, USA
thomas.knight@ngc.com

Ricardo Borges
Synopsys, Inc
Raleigh, NC, USA
ricardo.borges@synopsys.com

**These authors contributed equally to this publication.*

***Abstract*—We present a machine learning accelerated Atoms-to-Devices multi-scale simulation workflow for coupling device simulations at the atomistic and continuum levels, applied to design of devices for the THz regime. This workflow is applicable to different material systems and can easily allow for computational speedups of >20,000x for high-accuracy atomistic simulations, achieving rapid simulation times and workflow integration suitable for design and optimization. When predicting performance on an example Si-doped graphene transistor (Si-GFET) the workflow suggests that these devices could operate well into the THz range in RF applications.**

Keywords—machine learning, atomistic, TCAD, THz, ML-FF

I. INTRODUCTION

In this contribution we demonstrate a modelling approach enabling the virtual characterization of new material systems and devices for operation in the THz regime, with rapid simulation times and workflow integration suitable for design and optimization. See figure 1 for a graphical representation of the workflow. At the core of the project are the development and demonstration of machine learning (ML) techniques to significantly reduce the runtime of the atomic-scale modelling, and a methodology to extract from atomic-scale modelling the data and model parameters needed for Technology Computer-Aided Design (TCAD) simulations. The workflow presented is applicable to other material systems, including novel materials, and speedups achieved through these techniques can benefit commercial applications such as communications, and many others.

II. MACHINE-LEARNED FORCE FIELD

To leverage machine learning for atomistic simulation of graphene FET devices, we use the Moment Tensor Potential (MTP) formulation for ML-based force fields (ML-FF) [1], implemented in the Synopsys QuantumATK® software package [2]. This allows training against the more accurate, but also much more time-consuming, first-principles method of Density Functional Theory (DFT). In short, the MTP formalism allows for a direct mapping between the atomic structure and the potential energy surface of a system, allowing fast calculation of energies, forces and stress (EFS) as shown in figure 2.

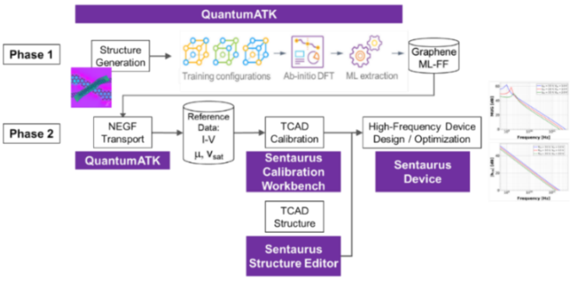

Figure 1: GFET Atoms-to-Devices multi-scale simulation flow

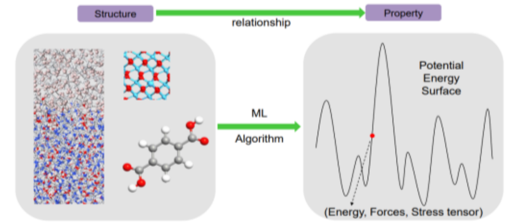

Figure 2: Illustration of MTP methodology which develops a machine-learned force field from a representation of the EFS for different structures

The DFT model parameters must be chosen to provide accurate structural information, providing a good reference for the MTP fitting, as well as being fast enough to make the NEGF (Non-Equilibrium Green's Function) IV calculations feasible. We chose DFT-LCAO (Linear Combination of Atomic Orbitals) with FHI (Fritz-Haber Institute) pseudopotentials and a DZP (Double-Zeta-Polarized) basis set, and the LDA (Local Density Approximation) exchange-correlation functional, which has been shown to work well for graphene on hexagonal boron-nitride (hBN) [3].

Using proprietary QuantumATK protocols to automatically expand input structures into training data sets, user-defined parameters are leveraged to target the MTP training data for the intended application. Anticipating that a bandgap in graphene would lead to better device designs relative to gapless pristine graphene, the training set included structures with silicon substitutions as such structures are theoretically predicted to open an energy gap in particular cases [4, 5]. Allowing inclusion of explicit substrate material in the later simulations requires incorporation of a substrate material at this earlier stage. We therefore include an hBN substrate beneath the Silicon-doped graphene layer during the training procedure.

The training set consists of 18 sub-groups of structures covering different sizes of supercells with different orientations between the two layers, different concentrations of silicon atoms, and different types of silicon defects. During the MTP training, several parameters, such as the cutoff radius and basis set size, were optimized to improve the agreement with the energy landscape's EFS values from DFT, to get the best possible MTP from the given training set.

Approved for Public Release, Distribution Unlimited; NG25-1114.
This material is based upon work supported by the Defense Advanced Research Projects Agency (DARPA) under Agreement No. HR00112390073

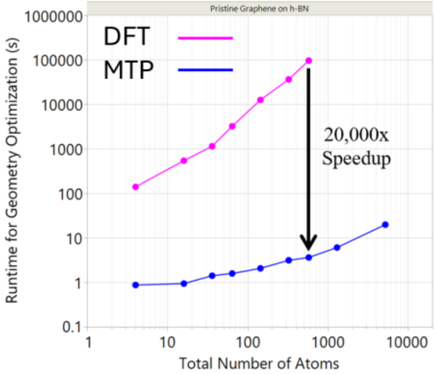

Figure 3: Example computational speedup of MTP relative to DFT for a geometry optimization. Depending on the physical observable of interest, even larger speedups can be achieved.

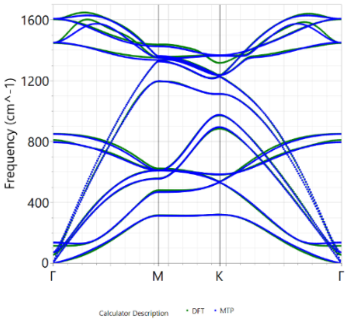

Figure 4: Illustration of a typical phonon bandstructure from an MTP (blue) and from the reference DFT calculator (green). Values were converted from energy units (eV) to frequency units (cm^{-1}) for comparison to literature by using a conversion factor of $h \cdot c$ which is approximately 0.124 meV/cm^{-1}. Good agreement is observed relative to the data of reference [6].

Overall we see over 97% accuracy in representing the selected physical observables relative to reference DFT calculations and computational speedups exceeding 20,000x for systems larger than 600 atoms, as shown in figure 3, thus demonstrating the potential for usage in multi-scale simulation flows where computational efficiency is required for design and optimization of device structures. In figure 4, we show how the phonon bandstructure of hBN-supported graphene is well reproduced by the MTP, which is crucial for using it to include electron-phonon coupling effects in the NEGF transport simulations.

III. ATOMISTIC TRANSPORT CALCULATIONS WITH NEGF

Using the MTP force field, we can include electron-phonon coupling effects in the atomistic transport simulation via the Special Thermal Displacement method, which would otherwise be prohibitively expensive, without the acceleration provided by the machine-learned force field. This allows us to calculate IV curves at finite temperatures with first-principles methods, providing a more realistic input for TCAD-level simulations for novel materials than what was previously achievable without this methodology.

The Special Thermal Displacement method creates a single atomic configuration with atomic displacements approximating a weighted superposition of the relevant phonon modes at a given temperature. For large systems with degenerate phonon modes, such as the device designs in this study, it is a good approximation and provides a very efficient way of including electron-phonon coupling in the atomistic transport calculations.

Using the same DFT model as described in the previous section on MTP training, we calculated IV curves of a silicon-doped graphene field-effect transistor (Si-GFET) for varying combinations of V_{GS} and V_{DS}. During the execution of the project, it became apparent that including an explicit atomic description of the hBN substrate did not differ significantly from describing it as a continuum dielectric, and we therefore prioritized increasing the size of the silicon-doped graphene over inclusion of explicit hBN for the NEGF simulations.

IV. NEGF TO TCAD

To demonstrate the multi-scale simulation flow depicted in figure 1, we link NEGF quantum transport simulations of the Si-GFET with subsequent TCAD-level simulations of static and small-signal RF behavior to explore their potential in high-speed THz RF applications.

The same dimensions, doping and Si content were used in TCAD simulations carried out with Sentaurus™ Device from Synopsys [7]. The only exception is that Sentaurus Device requires a finite effective thickness, t_{ch}, for the graphene monolayer. We also simply incorporate the 2.5 Å vacuum layers sandwiching the graphene monolayer to top and bottom hBN insulator thicknesses for simplicity and slightly reduce their dielectric constant for an equivalent insulator thickness. As the structure is symmetric in Sentaurus Device, we only simulate its upper half as shown in figure 5.

The choice of a good t_{ch} value that leads to approximate simulations of 2-D materials requires all solution variables to be as constant along the depth direction as possible so that they can be converted to 2-D solutions by simply multiplying them by t_{ch}. A simple approach to enforce constant potential along the depth of the channel is to artificially increase the off-plane component of the graphene dielectric constant, $\varepsilon_{\mathrm{Gr},\perp}$, so that $t_{\mathrm{ch}} \ll L_D$, the Debye length. As the inversion layer in the channel tends to grow larger than the electron density in the source/drain regions, we impose the stricter condition for the channel region under heavy inversion, which can be shown to obey:

$$\varepsilon_{\mathrm{Gr},\perp} \gg \frac{(V_{\mathrm{GS,max}} - V_{\mathrm{T}})}{u_{\mathrm{T}}} \varepsilon_{\mathrm{hBN}} \quad (1)$$

where u_{T} is the thermal potential, $\varepsilon_{\mathrm{hBN}}$ the hBN low frequency dielectric constant, $V_{\mathrm{GS,max}}$ the maximum gate voltage, and V_{T} the threshold voltage.

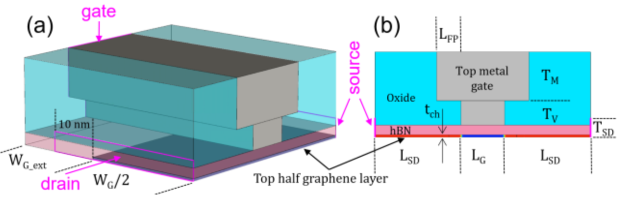

Figure 5: 3-D simulation structure with ¼ of the structure – half width and half height – and (b) transversal cross-section showing the top half of the graphene channel in the simulation domain.

Approved for Public Release, Distribution Unlimited; NG25-1114.
This material is based upon work supported by the Defense Advanced Research Projects Agency (DARPA) under Agreement No. HR00112390073

A. *TCAD Model Calibration*

To perform model calibration, we first extract $\varepsilon_{\mathrm{hBN}} \cong 2.0$ from QuantumATK, correct it to $\varepsilon_{\mathrm{hBN}} \cong 1.9$ to account for the 2.5 Å vacuum layer, and, assuming $\left(V_{\mathrm{GS,max}} - V_{\mathrm{T}}\right) < 1$ V, we compute a minimum value for $\varepsilon_{\mathrm{Gr},\perp,\mathrm{min}} \simeq 65$ at room temperature. Simulations of static and RF characteristics are not sensitive to the exact value of $\varepsilon_{\mathrm{Gr},\perp}$ if it is large enough and, as we want $t_{\mathrm{ch}} \ll L_{\mathrm{D,ch}}$, we arbitrarily set $\varepsilon_{\mathrm{Gr},\perp} = 300$.

We then need a good choice for an effective in-plane dielectric constant, $\varepsilon_{\mathrm{Gr},\parallel}$ to mimic the 2-D material electrostatics. Using the Poisson equation, it is possible to show that:

$$t_{\mathrm{ch}}\ \varepsilon_{\mathrm{Gr},\parallel} \cong 18 \times \frac{N_{\mathrm{D,2D}}}{\left|\left(\frac{\partial^2\varphi}{\partial x^2}\right)\right|}\ \ \mathrm{nm} \qquad (2)$$

where φ is the macroscopic electrostatic potential in source/drain depletion regions. We define the value for $\varepsilon_{\mathrm{Gr},\parallel}$ from a best second-order polynomial curvature fit to that of the Hartree Difference Potential (HDP) from NEGF, $(\partial^2\varphi/\partial x^2) \cong 1.2 \times 10^{12}\ \mathrm{V/cm^2}$, shown in figure 6 and focused on the source-side depletion region. Therefore, the coefficient of the second order term corresponds to half of the curvature $(\partial^2\varphi/\partial x^2)$. With $N_{\mathrm{D,2D}} = 1 \times 10^{13}\ \mathrm{cm^{-2}}$ by design, the product is $t_{\mathrm{ch}}\ \varepsilon_{\mathrm{Gr},\parallel} \cong 150\ \mathrm{nm}$. Simulation of IV results remain unchanged as long as the $t_{\mathrm{ch}}\ \varepsilon_{\mathrm{Gr},\parallel}$ product is constant. Therefore, we arbitrarily select $t_{\mathrm{ch}} = 1$ nm and $\varepsilon_{\mathrm{Gr},\parallel} = 150$.

The doping areal density in NEGF is translated to the volume density required in Sentaurus Device using $N_{\mathrm{D,3D}} = N_{\mathrm{D,2D}}/t_{\mathrm{ch}} = 1.0 \times 10^{20}\ \ \mathrm{cm^{-3}}$ for our choice of t_{ch}.

We continued the calibration process by adjusting an analytical 3-D Density-Of-States (DOS) model with non-parabolicity in TCAD that allowed for a good match to the DOS extracted from QuantumATK shown in figure 7. More specifically, we calibrate the effective mass, $m^* = 0.58$, and the non-parabolicity coefficient, $\alpha = 0.25$, of one single Γ-valley in the Multi-Valley DOS model in Sentaurus Device. As electron and hole DOS are approximately symmetric for graphene, we use the same extracted parameters for electron and hole DOS for simplicity and because holes play only a minor role in transport of this GFET. The QuantumATK DOS computation also gives us $E_{\mathrm{g}} \cong 0.55$ eV.

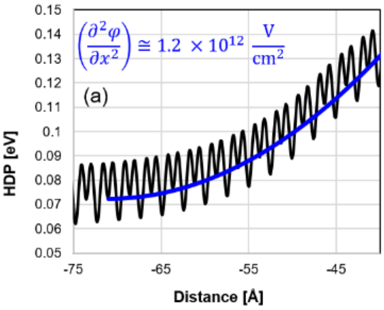

Figure 6: Hartree Differential Potential (HDP) zoomed in to depletion region on the source side with best curvature fit

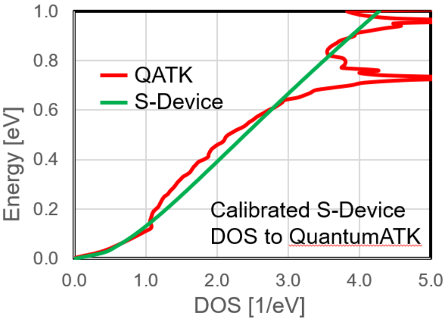

Figure 7: DOS vs. energy from QuantumATK and Sentaurus Device for 8.3% Si enriched graphene

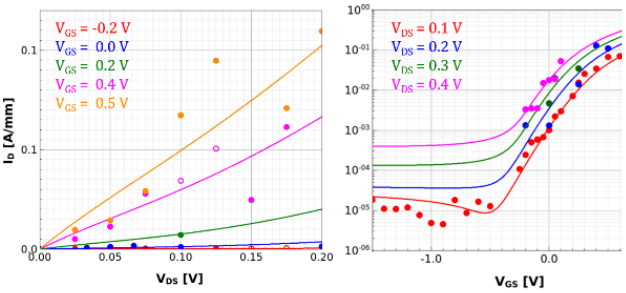

Figure 8: IdVd and IdVg curves for the device with $x_{\mathrm{Si}} \cong 8.3\%$. NEGF: Symbols; TCAD: lines

B. *IV Curves*

We ran NEGF and S-Device simulations of IdVd and IdVg curves for multiple $\mathrm{V_{DS}}$ values with corresponding results being shown in figure 8. Good match to NEGF is obtained with parameters shown in table 1 that includes a trivially adjusted constant mobility, where "constant" in this context means that it does not depend on any physical quantities such as the temperature or doping but still depends on the longitudinal electric field. A value, $\mu_n = 70\ \ \mathrm{cm^2/V\,s}$, produces a reasonable match in the entire range of $\mathrm{V_{GS}}$ and $\mathrm{V_{DS}}$ values probed. The large sub-threshold slope for all curves, $SS \cong 230\ \mathrm{mV/dec}$, is entirely explained by 2-D electrostatics and the $t_{\mathrm{ch}}\ \varepsilon_{\mathrm{Gr},\parallel}$ product, and does not require interface states or any other complex explanations. Also, the leakage current predicted by NEGF at large negative $\mathrm{V_{GS}}$ values can be matched by including one of the band-to-band models in simulations.

Comparison of results from NEGF and TCAD simulations allows us to estimate v_{Sat} within the range 10^7 to $1.0 \times 10^8\ \mathrm{cm/s}$. Extraction of a more-precise value could be improved with expanded $\mathrm{I_{DS}}$-$\mathrm{V_{DS}}$ data. On the other hand, our lower drain bias data fits well an experimental density-dependent v_{Sat} model proposed in [8] and we, therefore, used an identical model available in Sentaurus Device with parameters that fit the experimental dependence.

Table 1 summarizes model parameters employed in simulations of IV curves and RF analyses, with some of their final values fine-tuned to best match IV's from NEGF.

C. *TCAD Setup for High-Frequency Simulations*

Calibrated 3-D Sentaurus Device simulations for the structure depicted in Figure 5 are subsequently employed in the optimization of structural parameters of a Si-GFET with a T-gate. As parasitics, especially the distributed gate resistance, strongly affect $\mathrm{f_{Max}}$, we use full 3-D simulations in the optimization task. Although the initial calibration work did

Approved for Public Release, Distribution Unlimited; NG25-1114.
This material is based upon work supported by the Defense Advanced Research Projects Agency (DARPA) under Agreement No. HR00112390073

Table 1: Model parameters to match IVs from NEGF

Parameter	Symbol	Value	Unit
Bandgap	E_g	0.55	eV
Graphene anisotropic effective Dielectric Constant	$\epsilon_{\mathrm{Gr},\perp}$	300	-
	$\epsilon_{\mathrm{Gr},\parallel}$	150	-
Effective mass	m^*	0.58	-
DOS non-parabolicity coefficient	α	0.25	
hBN anisotropic Dielectric Constant	$\epsilon_{\mathrm{hBN},\perp}$	1.70	-
	$\epsilon_{\mathrm{hBN},\parallel}$	2.00	-
Gate metal work function	Φ_M	5.25	eV
Constant Mobility	μ_n	70	cm^2/V-s
Density-dependent saturation velocity	v_{Sat0}	1.5×10^8	cm/s
	b_{s0}	0.62	
	n_{s0}	3.9×10^{12}	cm^{-2}
Schenk Band-to-Band tunneling model	A	9.0×10^{24}	$\mathrm{cm^{-1}s^{-1}V^{-}}$
	B	2.2×10^7	$\mathrm{Vcm^{-1}eV^{-}}$
	$\hbar\omega$	18.6	meV

not include mobility doping dependence as that is not captured in NEGF, a realistic exploration of design space should include at least approximate source/drain series resistances, and that requires mobility doping dependence. Therefore, we employed a Si-like dependence in our simulations as there seems to be no experimental data for graphene available yet. Table 2 lists the structural parameters used in the optimization process. The parameters $\mathrm{T_V}$ and $\mathrm{T_M}$ influence input capacitance and gate resistance the most, if $\mathrm{W_G}$ and $\mathrm{L_G}$ are held fixed. In this work, we also fix other parameters in Table 2. The magnitude of drain bias, $V_{\mathrm{DS}} = 1.0\ \mathrm{V}$, was chosen based on similar values used in modern Si-based devices such as FinFETs or nanosheets that employ similar gate lengths as in the Si-GFET of this work.

The workflow for a Si-GFET model that accounts for multiple design parameters allowed us to explore the design space and suggests that it is possible to produce graphene-based FETs that could operate well into the THz frequency range as shown in figure 9 that plots $\mathrm{f_T}$ and $\mathrm{f_{Max}}$ vs. $\mathrm{V_{GS}}$ bias. For instance, the optimum values, $\mathrm{T_V} = 126\ \mathrm{nm}$, and $\mathrm{T_M} = 187\ \mathrm{nm}$ produce a device that exhibits $\mathrm{f_{Max}} \cong 2\ \mathrm{THz}$ according to Sentaurus Device simulations.

We realize that drain biases might be excessive for GFETs. Indeed, some leakage is present in simulated Si-GFETs due to band-to-band tunneling through the theoretical narrow bandgap opened by the introduction of Si in graphene. Nonetheless, that leakage would not play a significant role, e.g., if the Si-GFET was part of a class A RF power amplifier. Exploring the ($\mathrm{V_{GS}}$, $\mathrm{V_{DS}}$) bias space is a natural extension of this work.

Table 2: Structural parameter values for the optimization of RF performance figures of merit via 3D TCAD device simulations. Parameters $\mathrm{T_V}$ and $\mathrm{T_M}$ that characterize the gate metal geometry vary according to the intervals in the last two columns

$\mathrm{W_G}$ (µm)	$\mathrm{W_{G\_ext}}$ (nm)	$\mathrm{L_G}$ (nm)	$\mathrm{L_{SD}}$ (nm)	$\mathrm{T_{SD}}$ (nm)	$\mathrm{L_{FP}}$ (nm)	$\mathrm{T_V}$ (nm)	$\mathrm{T_M}$ (nm)
5.0	100	22.5	3.0	5.0	0.0	5-468	10-485

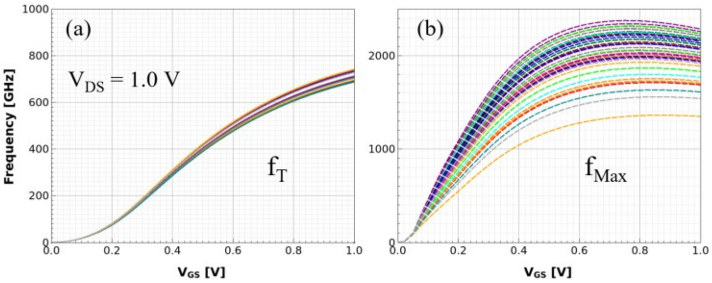

Figure 9: $\mathrm{f_T}$ (a) and $\mathrm{f_{Max}}$ (b) as a function of $\mathrm{V_{GS}}$ bias corresponding to different designs for the optimization of parameters listed in table 2.

V. CONCLUSION

We present a machine learning accelerated Atoms-to-Devices multi-scale simulation workflow for coupling device simulations at the atomistic and continuum levels. This workflow allows significant computational speedups while still preserving the accuracy of DFT simulations. As an example, we apply the workflow to a hypothetical Si-GFET and conclude that these devices could operate in RF THz range applications. Such techniques are not limited to RF applications or graphene and can be beneficial for investigating novel material systems for other applications.

REFERENCES

[1] A. Shapeev, “Moment Tensor Potentials: a class of systematically improvable interatomic potentials,” *Multiscale Modeling & Simulation*, vol. 14, no. 3, pp. 1153–1173, doi: https://doi.org/10.1137/15M1054183.

[2] S. Smidstrup *et al.*, “QuantumATK: an integrated platform of electronic and atomic-scale modelling tools,” *J. Phys.: Condens. Matter*, vol. 32, no. 1, p. 015901, Jan. 2020, doi: 10.1088/1361-648X/ab4007.

[3] F. Hüser, T. Olsen, and K. S. Thygesen, “Quasiparticle GW calculations for solids, molecules, and two-dimensional materials,” *Phys. Rev. B*, vol. 87, no. 23, p. 235132, Jun. 2013, doi: 10.1103/PhysRevB.87.235132.

[4] M. S. S. Azadeh, A. Kokabi, M. Hosseini, and M. Fardmanesh, “Tunable bandgap opening in the proposed structure of silicon-doped graphene,” *Micro & Nano Letters*, vol. 6, no. 8, pp. 582–585, Aug. 2011, doi: 10.1049/mnl.2011.0195.

[5] J. Charles, . Kais, and T. Kubis “Introducing Open Boundary Conditions in Modeling Nonperiodic Materials and Interfaces: The Impact of the Periodicity Assumption” ACS Materials Letters vol. 2 (3), pp. 247-253, 2020, DOI: 10.1021/acsmaterialslett.9b00523

[6] G. J. Slotman, G. A. de Wijs, A. Fasolino, and M. I. Katsnelson, “Phonons and electron-phonon coupling in graphene-h-BN heterostructures,” *Annalen der Physik*, vol. 526, no. 9–10, pp. 381–386, 2014, doi: 10.1002/andp.201400155.

[7] Synopsys’ Sentaurus Device User Guide, Version W-2024.09-SP1

[8] M. Yamoah, et. al., “High Velocity Saturation in Graphene Encapsulated by Hexagonal Boron Nitride”, ACS Nano 2017, 11, 9914-9919

This material is based upon work supported by the Defense Advanced Research Projects Agency (DARPA) under Agreement No. HR00112390073